ACS APPLIED MATERIALS & INTERFACES

Research Article

www.acsami.org

Carbon Quantum Dots Modified BiOCl Ultrathin Nanosheets with Enhanced Molecular Oxygen Activation Ability for Broad Spectrum Photocatalytic Properties and Mechanism Insight

Jun Di,[†] Jiexiang Xia,[*,†] Mengxia Ji,[†] Bin Wang,[†] Sheng Yin,[†] Qi Zhang,[†,§] Zhigang Chen,[‡] and Huaming Li[*,†]

[†]School of Chemistry and Chemical Engineering, Institute for Energy Research, and [‡]School of the Environment, Jiangsu University, 301 Xuefu Road, Zhenjiang, 212013, P. R. China

[§]Hainan Provincial Key Lab of Fine Chemistry, Hainan University, Haikou 570228, China

Supporting Information

ABSTRACT: In this paper, carbon quantum dots (CQDs) modified BiOCl ultrathin nanosheets photocatalyst was synthesized via a facile solvothermal method. The structures, morphologies, optical properties, and photocatalytic properties were investigated in detail. The photocatalytic activity of the obtained CQDs modified BiOCl ultrathin nanosheets photocatalyst was evaluated by the degradation of bisphenol A (BPA) and rhodamine B (RhB) under ultraviolet, visible, and near-infrared light irradiation. The CQDs/BiOCl materials exhibited significantly enhanced photocatalytic performance as compared with pure BiOCl and the 5 wt % CQDs/BiOCl materials displayed the best performance, which showed a broad spectrum of photocatalytic degradation activity. The main active species were determined to be hole and $O_2^{\bullet-}$ under visible light irradiation by electron spin resonance (ESR) analysis, XPS valence spectra, and free radicals trapping experiments. The crucial role of CQDs for the improved photocatalytic activity was mainly attributed to the superior electron transfer ability, enhanced light harvesting, and boosted catalytic active sites.

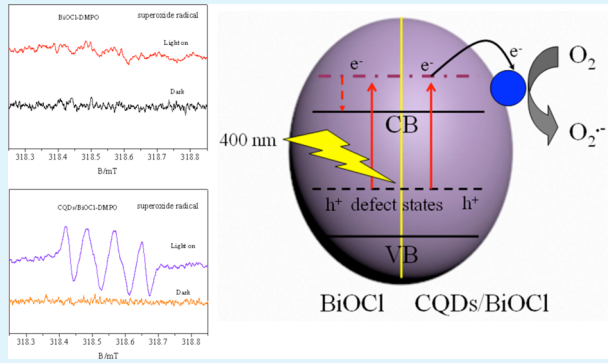

KEYWORDS: *CQDs, BiOCl, ultrathin nanosheets, photocatalytic mechanism*

1. INTRODUCTION

Along with the discovery of graphene, ultrathin two-dimensional materials have aroused increasingly research interest due to their fascinating properties[1] and have been applied in many fields such as photodetectors, thermoelectric conversion, touchless moisture sensing, supercapacitors, and lithium ion batteries.[2,3] For photocatalytic applications, the ultrathin two-dimensional inorganic materials with a suitable band gap may represent the ideal architecture for high-performance photocatalytic activity. The photoinduced charge carriers generated inside the semiconductor will take longer time to reach the surface with respect to the charge carriers produced approach to the surface.[4] When ultrathin semiconductor materials were constructed, the photogenerated carriers could transfer from the inside to the surface quickly. At the same time, the ultrathin structure would result in large fraction of uncoordinated surface atoms, which could harvest more ultraviolet−visible light.[4] Therefore, it is desirable to construct the ultrathin two-dimensional materials with a suitable band gap and applied in photocatalysis.

As a new promising layered material for photocatalytic energy conversion and environment remediation, bismuth oxychloride (BiOCl) has recently drawn much attentions.[5−7] This layered structure with interlacing $[Bi_2O_2]$ slabs with double chlorine slabs could produce self-built internal static electric fields that can promote the effective separation of photogenerated electron−hole pairs and thus result in the efficient photocatalytic activity.[8] Up to now, many strategies have been employed in order to acquire BiOCl materials with high photocatalytic activity, such as morphology control,[9,10] crystal facet exposure,[11,12] surface modification,[13−15] and coupling with other photocatalysts.[16−20] Among them, the controllable preparation of atomically ultrathin nanosheets may be a effective strategy. Based on the diffusion formula of $t = d^2/k^2D$ (d is the particle size, k is a constant, D is the diffusion coefficient of electron−hole pairs),[21] the atomically ultrathin thickness reduce the d value and the self-built internal static electric fields of layered BiOCl enlarge the D value.[6] Thus, the ultrathin BiOCl material could display improved separation efficiency of electron−hole pairs. However, it is still far from enough for potential applications and it is necessary to further improve the photocatalytic activity to meet the potential

Received: June 14, 2015
Accepted: August 11, 2015
Published: September 1, 2015

DOI: 10.1021/acsami.5b05268
ACS Appl. Mater. Interfaces 2015, 7, 20111−20123

industrial applications. The large-size materials could not construct perfect interfaces with BiOCl matrix and the surface defects among the interfaces may serve as recombination centers of electron−hole pairs. Intuitively, CQDs could be candidates to reduce the number of interfacial defects and increase the separation efficiency of electron−hole pairs.

Carbon quantum dots (CQDs), quasi-spherical nanoparticles usually <10 nm in diameter, can be amorphous or nanocrystalline with sp^2 carbon clusters and may fused with some diamond-like structure formed by sp^3 carbons.[22] They display excellent aqueous solubility, high biocompatibility, low cytotoxicity, tunable photoluminescence and have been successfully utilized in biosensing, bioimaging, nanomedicine, and electrocatalysis.[23] Very recently, CQDs have been introduced to photocatalytic applications due to the superior electron transfer ability. Several photocatalytic systems based on the CQDs have been studied and the enhanced activity was obtained, such as CQDs/TiO_2,[24−27] CQDs/Ag_3PO_4,[28] CQDs/C_3N_4,[29] CQDs/Cu_2O,[30] and CQDs/Bi_2WO_6.[31] However, the structure−activity relationships and the crucial role of CQDs for the improved photocatalytic activity are still need to be further explored. Considering the fact that CQDs are small-sized, the interface mismatch between the CQDs and BiOCl ultrathin nanosheets can be minimized, and nanoscale heterojunctions with intimate contacts can be constructed. This unique nanostructure has some advantages. It can increase the accessible area of the CQDs and BiOCl planar interface and the bulk-to-surface channels for the electrons can be constructed, thus accelerating the interfacial charge transfer process. Also, the highly dispersed CQDs can reduce the light blocking effect, so that adequate light can access BiOCl materials and enabling the efficient light utilization.[32] Some systems have demonstrated the nanoscale heterojunctions with intimate interface could greatly enhanced the separation of electron−hole pairs.[33−37] Inspired from the aforementioned concepts, it is highly desirable to construct the architecture of CQDs modified on the BiOCl ultrathin nanosheets in order to achieve efficient photocatalysis application.

In this work, we prepared novel CQDs modified BiOCl ultrathin nanosheets photocatalyst via a solvothermal method. The structures, morphologies, optical properties and photocatalytic properties were investigated in detail. Through the photocatalytic activity evaluation by the degradation of BPA and RhB under ultraviolet, visible, and near-infrared light irradiation, it was demonstrated that CQDs modification was an effective approach to improve the photocatalytic performance. The structure−activity relationships have been studied in details. The active species was determined and photocatalytic mechanism was proposed.

2. EXPERIMENTAL SECTION

2.1. Photocatalyst Synthesis. All of the reagents were analytical grade and were used as received. The CQDs solid was prepared based on the literature and then handled by freeze-drying.[38] A 5 mmol portion of citric acid was dissolved in 10 mL deionized water and 335 μL ethylenediamine was then added. The above solution was transferred into 25 mL Teflon-lined autoclave and heated at 200 °C for 5 h and cooled down to room temperature. The acquired product was subjected to dialysis for 24 h in order to obtain the CQDs solution. Then the CQDs solution was handled by freeze-drying for 48 h to obtain the CQDs solid.

The CQDs modified BiOCl ultrathin nanosheets were synthesized according to the literatures[9,10] and make a modification. In a typical synthesis of CQDs modified BiOCl ultrathin nanosheets materials, 0.5 mmol $Bi(NO_3)_3{\cdot}5H_2O$ was initially dissolved in 15 mL mannitol solution (0.1 M) under magnetic stirring at room temperature. Then 0.2 g PVP and a certain amount of CQDs were added into above solution and defined as solution A. 0.5 mmol NaCl was dissolved into 5 mL H_2O to obtain solution B. The solution B was dropwise added into solution A under stirring. After being stirred for 30 min, the suspension was added into 25 mL Teflon-lined autoclave and subsequently heated at 160 °C for 3 h. The reactor was then allowed to cool to room temperature naturally and the precipitate was collected and washed with deionized water and ethanol for four times, and the final products dried at 50 °C for 12 h. The added contents of CQDs in the CQDs/BiOCl materials were 3, 5, and 8 wt %, respectively.

2.2. Photocatalyst Characterization. The crystal structures and phase data for the photocatalysts were determined by X-ray diffractometry (XRD) using a Bruker D8 diffractometer with Cu Kα radiation. The chemical states of the prepared samples were analyzed by X-ray photoelectron spectroscopy (XPS) using a VG MultiLab 2000 system with a monochromatic Mg−Kα source operated at 20 kV. The morphology of the samples was investigated by scanning electron microscope (SEM) (JEOL JSM-7001F) equipped with an energy-dispersive X-ray spectroscope, as well as by transmission electron microscopy (TEM) (JEOL-JEM-2010). The UV−vis spectra in this system were obtained via a UV−vis spectrometer (Shimadzu UV-2450 spectrophotometer) by diffuse reflectance method with $BaSO_4$ powder as the substrate. A certain amount of photocatalyst was mixed with the $BaSO_4$ and then tabletting for measuring. The Tauc equation was then used to calculate the band gap of BiOCl materials. Surface areas of the samples were determined using Brunauer−Emmett−Teller (BET) method based on the N_2 adsorption−desorption isotherms collected on a TriStar II 3020 surface area and porosity analyzer (Micromeritics Instrument Corporation, USA). The photoluminescence (PL) spectra of the prepared samples were detected using a Varian Cary Eclipse spectrometer. Electron spin resonance (ESR) spectra were conducted on a Bruker model ESR JES-FA200 spectrometer. The electrochemical experimental results were recorded with a CHI 660B electrochemical system with a constructed three electrode system. Pt wire was used as a counter electrode and Ag/AgCl/sat. KCl was used as a reference electrode, while the thin film on ITO was used as the working electrode for investigation. The photocurrent was carried out in phosphate buffer solution (PBS, 0.1 M, pH 7.0), and the electrochemical impedance spectroscopy (EIS) was performed in a 0.1 M KCl solution containing 5 mM $Fe(CN)_6^{3-}/Fe(CN)_6^{4-}$.

2.3. Photocatalytic Activity Test. The photocatalytic activity of the as-prepared CQDs/BiOCl materials were investigated by the photodegradation of rhodamine B (RhB, 10 mg/L) and bisphenol A (BPA, 10 mg/L). Then, 20 and 50 mg CQDs/BiOCl samples were added in the different Pyrex photocatalytic reactors for the degradation of 100 mL RhB and 100 mL BPA, respectively. A 250 W high pressure Hg lamp was used as the UV source. A 300 W Xe arc lamp was used as light source with a UV cutoff filter (400 nm) to provide the visible light and a 580 nm cutoff filter to provide the near-infrared light. The photocatalytic experiments were carried out at 30 °C with a circulating water system to prevent thermal catalytic effects. Prior to irradiation, the suspension was stirred in the dark for 30 min to ensure adsorption−desorption equilibrium. During irradiation, 3 mL suspension was sampled at certain time intervals and centrifuged at 13000 rpm for 3 min to remove the catalyst particulates for analysis. The filtrates of RhB degradation were analyzed by a UV−vis spectrophotometer (UV-2450, Shimadzu) at wavelength 553 nm. The remnant amount of BPA was analyzed by using high performance liquid chromatography (HPLC), which equipped with two Varian ProStar 210 pumps, an Agilent TC-C (18) column, and a Varian ProStar 325 UV−vis Detector at 230 nm. A solution of methanol and H_2O in the ratio 75:25 (v/v) was used as the mobile phase at 1 mL min^{-1}, and 20 μL of the sample was injected.

DOI: 10.1021/acsami.5b05268
ACS Appl. Mater. Interfaces 2015, 7, 20111−20123

3. RESULTS AND DISCUSSION

The photocatalytic activity of the as-prepared CQDs/BiOCl materials was first evaluated for the degradation of rhodamine B (RhB) in water under visible light irradiation (Figure 1a).

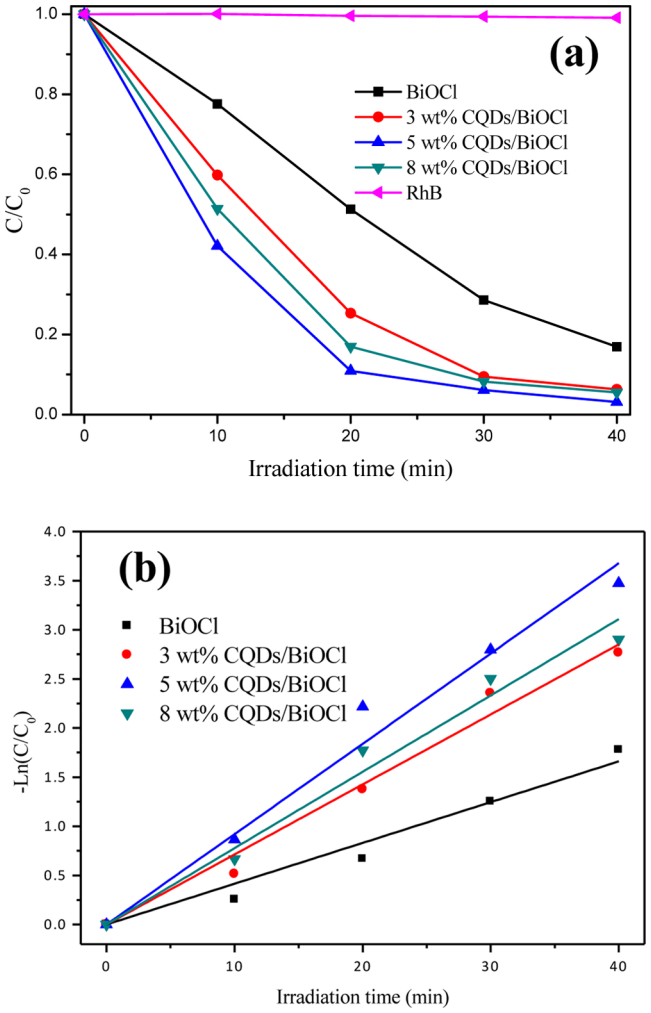

Figure 1. (a) Photocatalytic degradation of RhB in the presence of BiOCl, CQDs/BiOCl, and photolysis of RhB under visible light irradiation. (b) Kinetic fit for the degradation of RhB with the pure BiOCl and CQDs/BiOCl samples.

Before the photodegradation process, blank experiment was carried out without adding photocatalyst. It can be seen that the direct photolysis of RhB was negligible under visible light irradiation. As shown in Figure 1a, 49% RhB can be removed by pure BiOCl materials after 20 min irradiation. When the CQDs was introduced to the BiOCl materials, the photocatalytic activity greatly improved. The 5 wt % CQDs/BiOCl materials displayed the highest photocatalytic activity, which has a 40% improvement compared to pure BiOCl materials after 20 min irradiation. When the CQDs content was higher than 5 wt %, a further increase of CQDs content caused a decrease for the photocatalytic activity. Although the modification of CQDs to BiOCl was beneficial for charge transfer from the BiOCl matrix to CQDs, but too many CQDs cover on the surface of BiOCl would limit the light absorption of BiOCl. Similar results can also been found in the literatures.[31,39] In order to test the stability of the CQDs/BiOCl materials, the 5 wt % CQDs/BiOCl material was collected after RhB photodegradation experiment under visible light irradiation. As shown in Figure S1, the photocatalytic activity could still be maintained after four cycles with only 2.2% decrease of the degradation efficiency, which revealing the CQDs/BiOCl material has high stability during the photocatalysis process. The photocatalytic degradation kinetics of RhB under visible light irradiation was investigated, and was found the changes of the RhB concentration versus the reaction time over the CQDs/BiOCl materials followed pseudo-first-order kinetics plot by the equation of $-\ln(C/C_0) = kt$ (Figure 1b). The k value was the pseudo-first-order rate constant, C_0, and C were the RhB concentrations in solution at times 0 and t, respectively. It can be seen that the 5 wt % CQDs/BiOCl materials has the maximum rate constant of 0.0920 min^{-1}, which was 2.217 times higher than pure BiOCl. The relative coefficients and rate constants were summarized in Table S1.

Moreover, colorless model organic pollutant bisphenol A (BPA) was chosen to further evaluate photocatalytic activity of CQDs/BiOCl materials. BPA, which has been widely used for the production of many plastics products, has been regarded as an endocrine disrupting chemical (EDC). The toxicity tests illustrated that it may leading to various adverse effects on aquatic organisms even at low exposure levels.[40] The CQDs/BiOCl materials have been used to explore the BPA removing under the visible light irradiation and the result was shown in Figure 2a. It can be seen that 64.6% of BPA has been degraded over pure BiOCl under visible light irradiation for 120 min. It indicated that BiOCl material was an efficient photocatalyst for BPA degradation. After the CQDs was introduced, the CQDs/BiOCl materials displayed a higher activity for the degradation of BPA when compared with BiOCl, which could have an improvement of about 27%. The detailed degradation process of BPA in the presence of pure BiOCl and 5 wt % CQDs/BiOCl materials were shown in Figure 2b and Figure 2c. The photocatalytic degradation kinetics of BPA under visible light irradiation was investigated and also followed pseudo-first-order kinetics plot (Figure 2d). The rate constant of pure BiOCl and 5 wt % CQDs/BiOCl materials was 0.0089 and 0.0189 min^{-1}, respectively. The rate constant for 5 wt % CQDs/BiOCl was 2.124 times as high as that of pure BiOCl, which was similar for the RhB degradation. Consider the colorless of BPA, it indicated that the dye sensitization was not the main factor for the pollutant photodegradation in this system. The photocatalysis results suggested that the visible light reactivity of BiOCl materials might be associated with some other factors because the wide band gap of BiOCl and BPA cannot absorb the visible light. Therefore, the intrinsic reasons need to be clarified.

The photocatalytic performance of pure BiOCl and CQDs/BiOCl materials was further explore under the irradiation of ultraviolet and near-infrared light. As the Figure 3a shown, only 48% RhB can be photodegraded by BiOCl after 120 min under ultraviolet light irradiation. After the modification of CQDs, the photocatalytic activity was significantly improved and 91% RhB was photodegraded by CQDs/BiOCl materials under the same condition. Under the near-infrared light irradiation, (Figure 3b) the CQDs/BiOCl materials also exhibited higher activity than BiOCl, and 24% and 40% RhB can be photodegraded by pure BiOCl and CQDs/BiOCl materials, respectively. This indicated that the CQDs also play an important role for the enhancement of photocatalytic performance under the irradiation of ultraviolet and near-infrared light.

DOI: 10.1021/acsami.5b05268
ACS Appl. Mater. Interfaces 2015, 7, 20111−20123

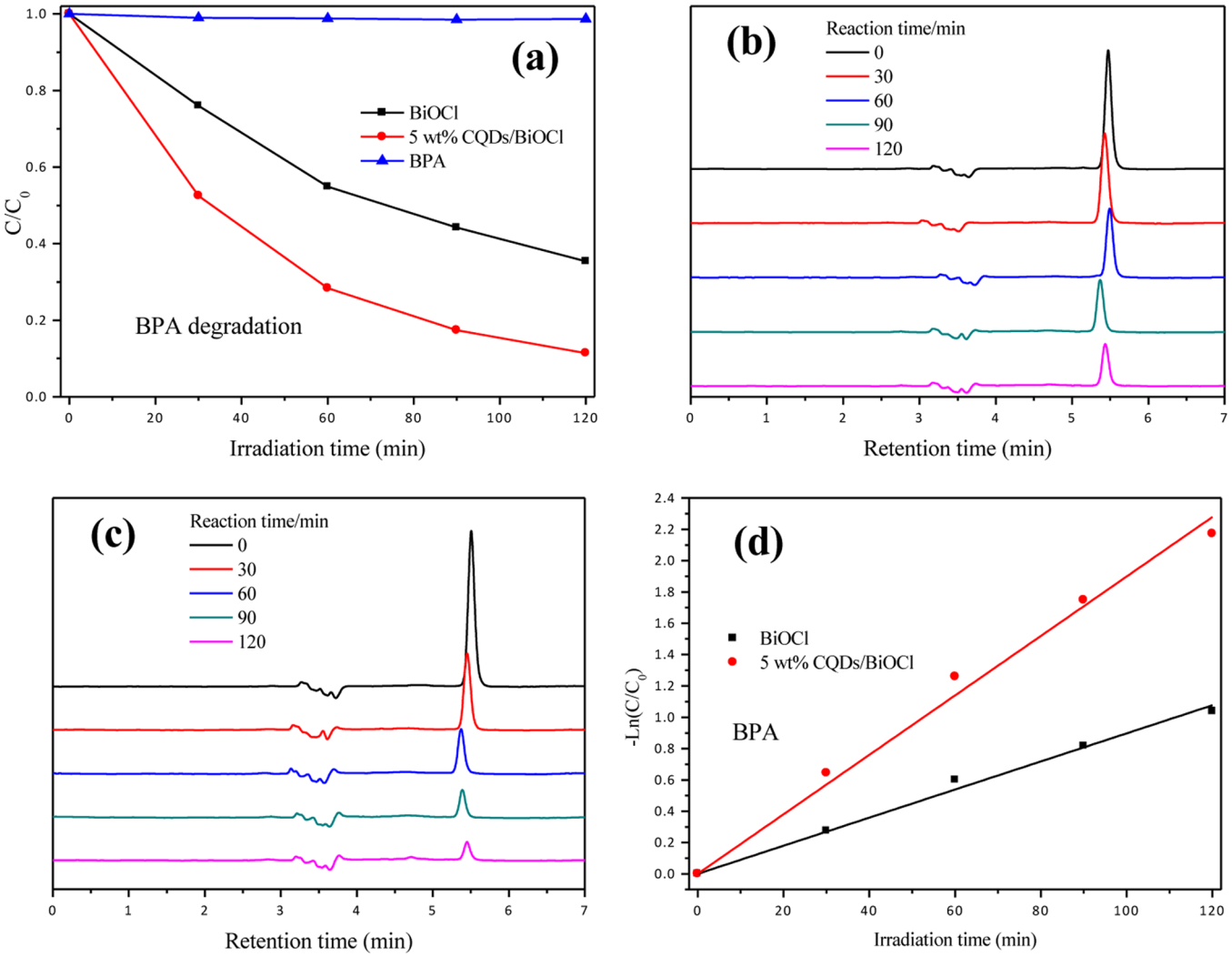

Figure 2. (a) Photocatalytic degradation of BPA in the presence of BiOCl, 5 wt % CQDs/BiOCl under visible light irradiation; HPLC chromatograms of the BPA degradation by using of (b) pure BiOCl and (c) 5 wt % CQDs/BiOCl under visible light irradiation. (d) Kinetic fit for the degradation of BPA with the pure BiOCl and 5 wt % CQDs/BiOCl samples.

The photocatalytic degradation kinetics of RhB under ultraviolet and near-infrared light irradiation were according with the pseudo-first-order kinetics plot (Figure 3c and d). The rate constant for 5 wt % CQDs/BiOCl was 3.887 times and 1.934 times higher than pure BiOCl under ultraviolet and near-infrared light irradiation, respectively. The ratio of rate constant for 5 wt % CQDs/BiOCl to pure BiOCl under near-infrared light irradiation was similar to the ratio under visible light irradiation, which indicated the similar activation pattern. Compared to visible light condition, the ratio of rate constant for 5 wt % CQDs/BiOCl to pure BiOCl under ultraviolet light condition was larger, which indicating the CQDs could transfer photogenerated electrons more efficiently under ultraviolet light. The different activity enhanced ability of CQDs was attributed to the different electronegativity of photogenerated electrons under various light irradiations.

The phase structures of the obtained samples were examined by X-ray diffraction (XRD) analysis. As shown in Figure 4, the as-prepared samples displayed the diffraction peaks of (0 0 1), (0 1 1), (1 1 0), (0 1 2), (1 1 2), (0 2 0), (1 1 3), (1 2 1), (1 2 2), (2 2 0), and (1 3 0) planes at 2θ = 12.0°, 25.9°, 32.6°, 33.6°, 41.0°, 46.8°, 49.9°, 54.2°, 58.8°, 68.3°, and 77.7°, which can be indexed to tetragonal phase of BiOCl (JCPDS card no. 73-2060). However, in the case of the CQDs/BiOCl materials, no diffraction peak of CQDs can be observed, which was due to its limited amount in the CQDs/BiOCl materials.[28,31]

X-ray photoelectron spectroscopy (XPS) was used to investigate the chemical states of BiOCl and CQDs/BiOCl materials. Figure 5a was the survey scan XPS spectrum, which clearly indicated that the BiOCl and CQDs/BiOCl samples were mainly composed of Bi, O, Cl, and C elements. Figure 5b showed the binding energies of Bi 4f7/2 and Bi 4f5/2 peaks in the BiOCl materials were located at 158.4 and 163.8 eV, respectively, suggesting the Bi^{3+} in the crystal structure.[41] The Bi 4f peak in the CQDs/BiOCl sample displayed a slight shift toward higher binding energies as compared to the Bi 4f peak in the pure BiOCl materials due to the interaction between CQDs and BiOCl. The O 1s peak at 529.3 eV (Figure 5c) was attributed to the oxygen in BiOCl materials. The Cl 2p high-resolution XPS spectrum showed two major peaks with binding energies at 197.1 and 198.5 eV, which could be ascribed to Cl 2p3/2 and Cl 2p1/2 of Cl^-, respectively (Figure 5d).[12] Figure 5e showed the high-resolution XPS spectra of C 1s, which revealed the surface functional groups on the CQDs. The main peak at 284.7 eV was attributed to the C−C bond with sp^2 orbital and the peaks centered at the binding energies of 286.0

DOI: 10.1021/acsami.5b05268
ACS Appl. Mater. Interfaces 2015, 7, 20111−20123

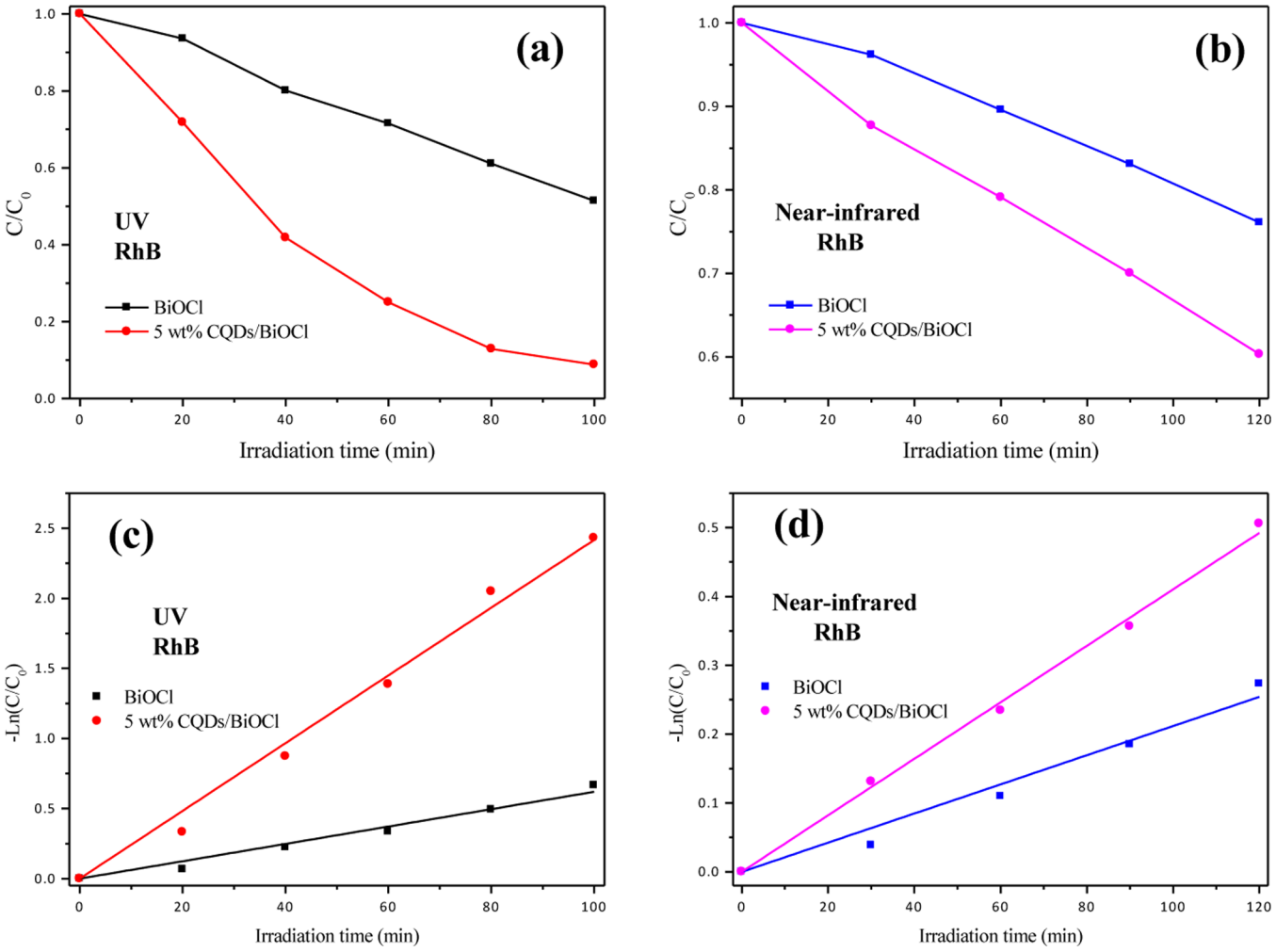

Figure 3. Photocatalytic degradation of RhB in the presence of BiOCl, 5 wt % CQDs/BiOCl materials under (a) ultraviolet light irradiation and (b) near-infrared light irradiation; Kinetic fit for the degradation of RhB with the pure BiOCl and 5 wt % CQDs/BiOCl materials under (c) ultraviolet light irradiation and (d) near-infrared light irradiation.

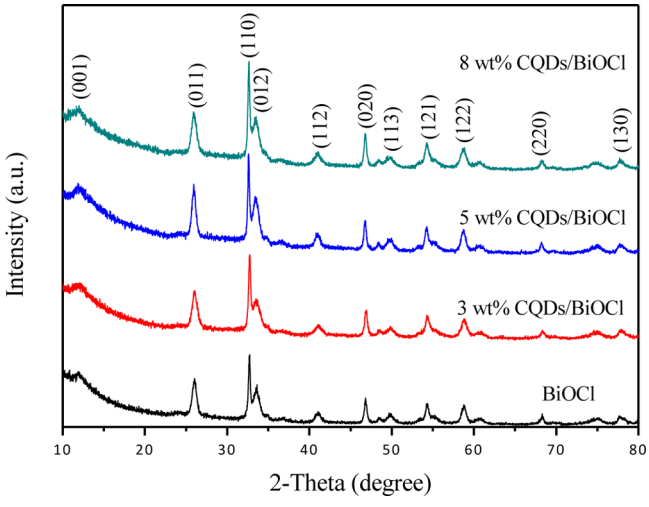

Figure 4. XRD pattern of the as-prepared CQDs/BiOCl materials.

and 287.5 eV were assigned to the oxygenated carbon and nitrous carbon, respectively.[38] The result of XPS analysis indicated the coexistence of BiOCl and CQDs in the CQDs/BiOCl materials.

The morphology and microstructure of the CQDs/BiOCl materials were investigated by the field emission scanning electron microscope (SEM) and the transmission electron microscopy (TEM). From Figure 6a, it can be seen that the as-prepared CQDs/BiOCl materials were numerous nanosheets with the size less than 100 nm. From the high-powered scanning electron micrograph Figure 6b, the ultrathin structure can be seen via the erected nanosheets. TEM analysis was applied to further explore the microstructure of CQDs/BiOCl materials (Figure 6c and d). The near transparency of the sheets implied the ultrathin structure and the thickness was determined to be ca. 2 nm. Numerous nanodots with the diameter about 2−3 nm can be seen, which indicated the CQDs have been coupled with the BiOCl in the nanoscale successfully. Figure 6e showed the HRTEM image of CQDs/BiOCl materials. The lattice spacing of BiOCl was determined to be 0.275 nm, which corresponding to the (110) crystal plane. The angle of two sets of lattice fringes was 90°, which was identical to the theoretical value for the angle between the (110) and (110) facets and further reveal that the exposed crystal facet was (001) facet. Some nanodots with diameter about 2−3 nm were evenly attached to the surface of BiOCl nanosheets, which revealing the CQDs have been modified on the BiOCl nanosheets to form well combination. The lattice

DOI: 10.1021/acsami.5b05268
ACS Appl. Mater. Interfaces 2015, 7, 20111−20123

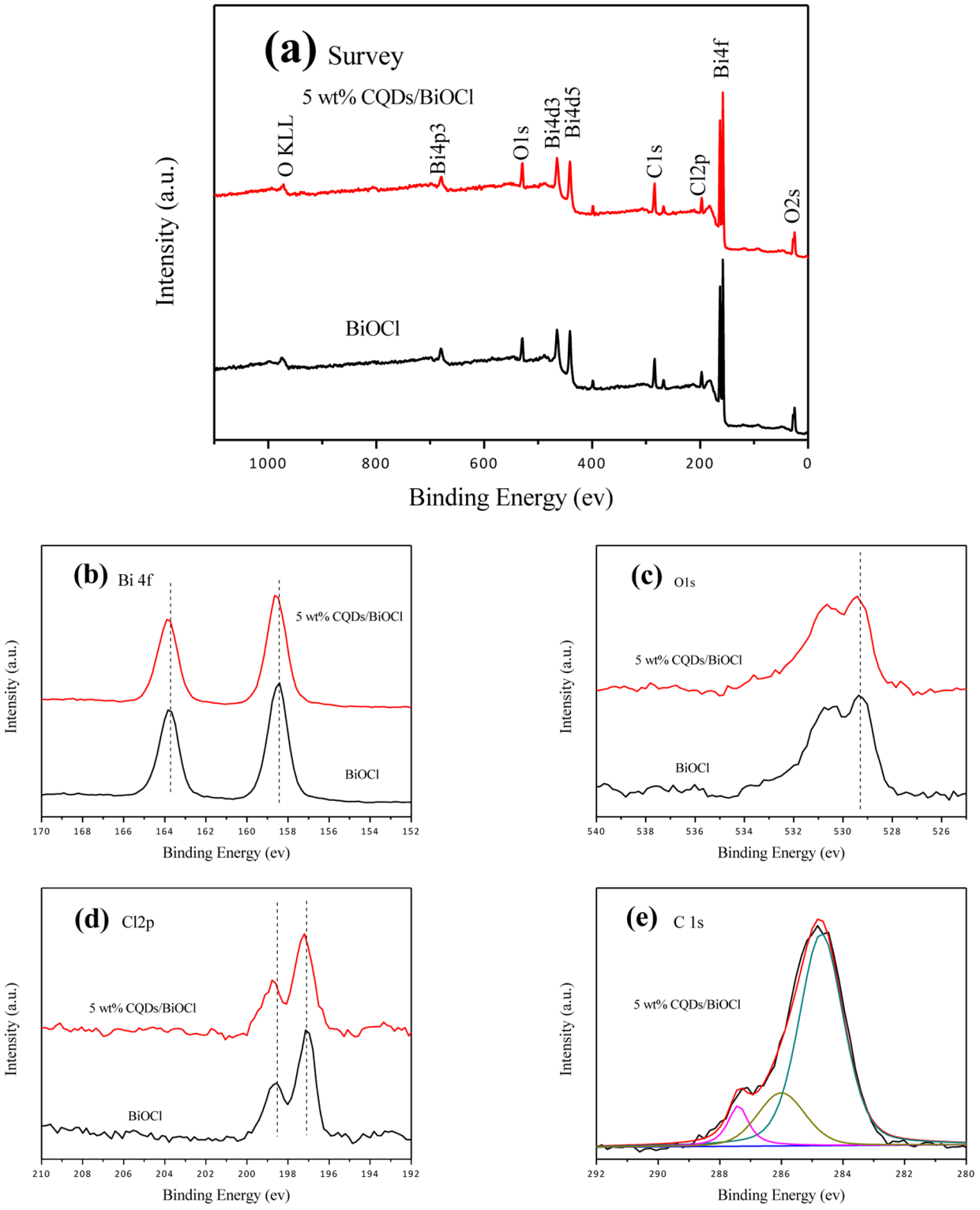

Figure 5. XPS spectra of CQDs/BiOCl materials. (a) Survey of the sample; (b) Bi 4f; (c) O 1s; (d) Cl 2p; (e) C 1s.

fringe spacing of CQDs cannot be observed and this was due to that CQDs were quasi-spherical nanoparticles comprising amorphous to nanocrystalline cores.[22] EDS element mapping clearly showed the elements Bi, Cl, O and C evenly distributed in CQDs modified BiOCl materials (Figure S2). The CQD content is about 4.31 wt % in the 5 wt % CQD/BiOCl materials.

The optical absorption of the BiOCl and CQDs/BiOCl samples were investigated by using UV−vis spectrometer. As shown in Figure 7, the BiOCl sample only has photoabsorption at UV light region, and the absorption edge was 360 nm. After the surface of BiOCl nanosheets was modified with CQDs, the obtained CQDs/BiOCl samples exhibited wide visible-light absorption region and enhanced light absorption intensity. The result indicated that the CQDs modified BiOCl samples can be

DOI: 10.1021/acsami.5b05268
ACS Appl. Mater. Interfaces 2015, 7, 20111−20123

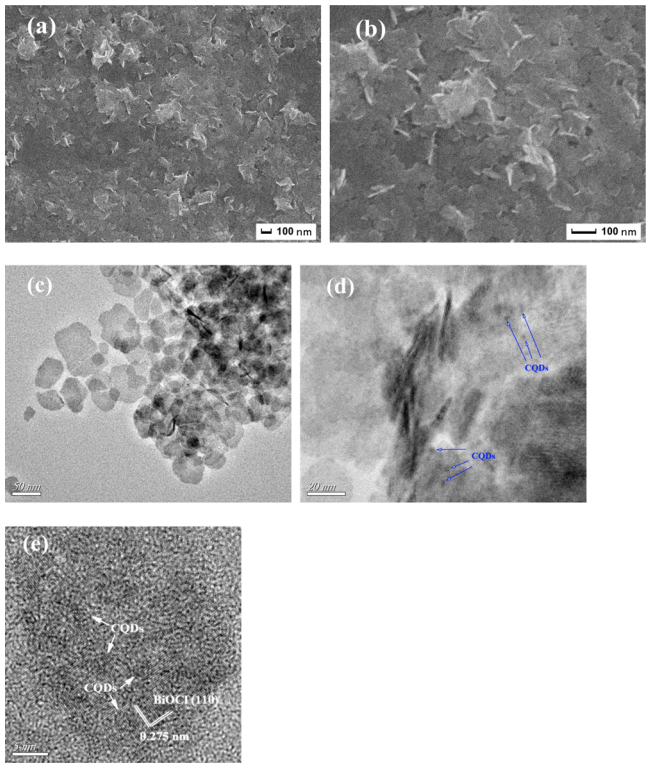

Figure 6. SEM and TEM images of the 5 wt % CQDs/BiOCl: (a, b) SEM images; (c, d) low magnification TEM images; (e) high magnification TEM image.

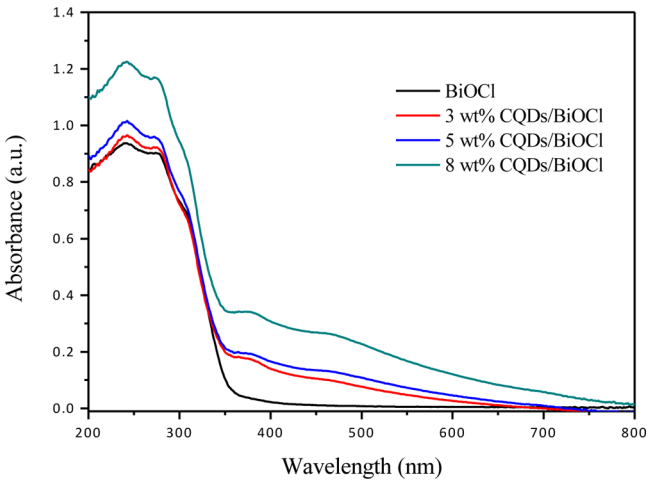

Figure 7. Optical absorption spectroscopy of CQDs/BiOCl materials.

excited to produce more electron−hole pairs under the same light irradiation, which could result in higher photocatalytic activity.[42]

The specific surface area of the as-prepared samples was investigated using nitrogen adsorption−desorption analysis (Figure 8). Type IV isotherms were observed, indicating the presence of mesopores (2−50 nm) formed between BiOCl nanosheets.[43] In comparison to the BiOCl nanosheets (31.96 $m^2\ g^{-1}$), the BET surface area of the CQDs modified BiOCl samples was smaller (23.87 $m^2\ g^{-1}$ for 3 wt % CQDs/BiOCl, 17.68 $m^2\ g^{-1}$ for 5 wt % CQDs/BiOCl and 9.94 $m^2\ g^{-1}$ for 8 wt % CQDs/BiOCl). It has been widely recognized that a higher BET surface area could enable absorb more active species and reactants on their surface and, thus, resulted in higher photocatalytic activity.[44] In this system, the modification of CQDs leading to the reduction of BET surface area, which revealing the specific surface area was not the main factor to responsible for the enhanced photocatalytic activity of CQDs/BiOCl materials.

Photoluminescence (PL) techniques were employed to investigate the transfer and recombination processes of photoinduced electrons and holes in BiOCl and CQDs/BiOCl samples. Figure 9a showed the steady-state PL spectra of the pure BiOCl and 5 wt % CQDs/BiOCl samples. The PL intensity with higher value stands for higher recombination possibility of electron−hole pairs. As shown in Figure 9a, pure BiOCl excited at 360 nm had a strong emission peak centered at about 468 nm. For CQDs/BiOCl material, the emission intensity was much lower than that of pure BiOCl at similar emission position, which meaning the modification of CQDs could effective reduce the recombination of electron−hole pairs.[45] The time-resolved transient PL spectra was employed to further exam the pure BiOCl and CQDs/BiOCl samples, as shown in Figure 9b. The lifetime of charge carriers in 5 wt % CQDs/BiOCl materials was longer than that in pure BiOCl. A longer PL lifetime meant a lower recombination rate of the electron−hole pairs, which was consistent with the steady-state PL analysis.

Electrochemical impedance spectroscopy (EIS) was a fundamental tool for characterizing the interfacial charge transfer properties of electrodes. Generally, the diameter of the semicircle in the Nyquist plot was equal to the charge transfer resistance of the electrode surface and a smaller diameter means a lower resistance.[46] Figure 10a displayed the Nyquist plot for the prepared BiOCl and CQDs/BiOCl samples. It was found that CQDs/BiOCl has a low resistance value as compared to BiOCl, that was consistent with the above results of PL analysis. It meant that a faster interfacial charge transfer to the electron acceptor occurs and leading to effective separation of electron−hole pairs by the introduction of CQDs.[47]

For better understanding, transient photocurrent was also performed. The prompt photocurrent response of the as-prepared materials corresponded well with on/off cycles of visible light irradiation (Figure 10b). A significantly higher photocurrent was seen for CQDs/BiOCl electrode in comparison to BiOCl electrode. It indicated the electron transfer from BiOCl to CQDs upon irradiation favored effective charge separation[48] and was in accordance with the above PL and EIS analysis.

The electron spin resonance (ESR) spin-trap technique was then performed to investigate the active species generated by using BiOCl and CQDs/BiOCl materials during the photodegradation process under visible light irradiation.[49] As the Figure 11a shows, the feeble characteristic peaks of DMPO-superoxide radical ($O_2^{\bullet-}$) were observed for the BiOCl material under the visible light irradiation, which indicated that only bits of $O_2^{\bullet-}$ was produced on the surface of visible light-irradiated BiOCl materials. While the DMPO-hydroxyl radical (·OH) species were not detected and it can be inferred that the ·OH was not the main reactive species (Figure 11b). For the CQDs/BiOCl materials, the intensity of DMPO-$O_2^{\bullet-}$ signals was much higher than that of BiOCl (Figure 11c). Due to the $O_2^{\bullet-}$ was generated through O_2 reduction via one-electron transfer, the higher $O_2^{\bullet-}$ intensity of CQDs/BiOCl materials revealing the introduction of CQDs enable the more photogenerated

DOI: 10.1021/acsami.5b05268
ACS Appl. Mater. Interfaces 2015, 7, 20111−20123

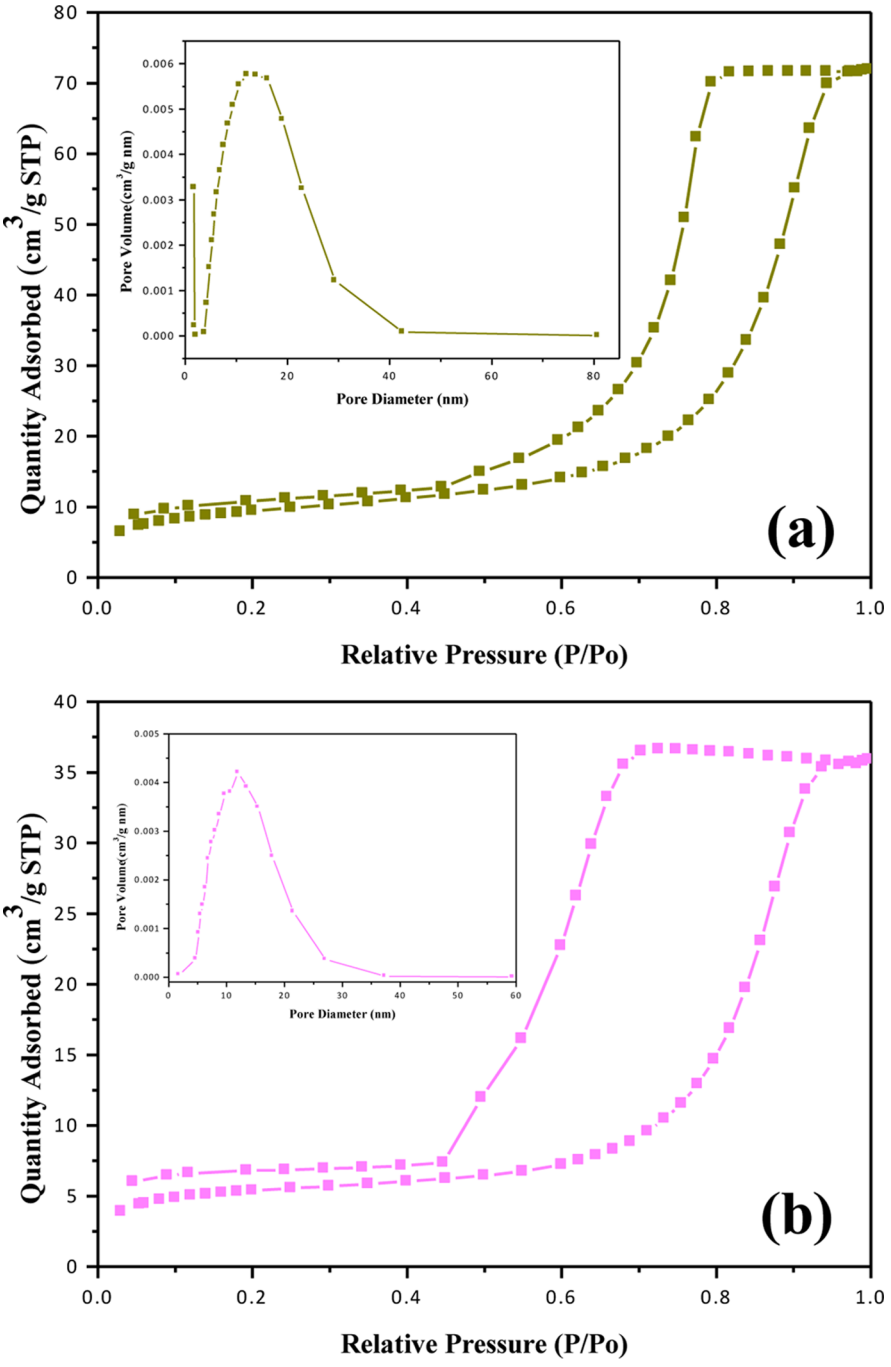

Figure 8. Nitrogen absorption−desorption isotherm of (a) pure BiOCl and (b) 5 wt % CQDs/BiOCl materials.

electrons to reduce O_2. This was attributed to the delocalized conjugated structure of CQDs making it easier to transfer the photogenerated electrons, resulting in efficient electron−hole pair separation. Similar to the BiOCl, ·OH was also not the main reactive species for CQDs/BiOCl materials (Figure 11d).

To further reveal the roles of the active species on the photocatalysis process over CQDs/BiOCl materials, a series of experiments were then carried out through adding different scavengers (tert-butanol and isopropyl alcohol (IPA) for ·OH p-benzoquinone (BQ) for $O_2^{\bullet-}$, ammonium oxalate (AO) and disodium ethylenediaminetetraacetate (EDTA-2Na) for holes).[50] As shown in Figure 12, when the tert-butanol and IPA was added, the photodegradation efficiency was not obvious affected, which indicated that the ·OH was not the main active species. However, when the BQ, AO, or EDTA-2Na was added, the degradation efficiency was great inhibited. This result implied the $O_2^{\bullet-}$ and holes were main active species during the photocatalysis process. The valence band (VB) and conduction band (CB) potentials were first calculated by using empirical equation. The VB potentials of BiOCl material was estimated by using the following empirical equation: $E_{VB} = X - E^e + 0.5E_g$.[51] The E_{VB} was the valence band edge potential, X is the electronegativity of the semiconductor, which was the geometric mean of the electronegativity of the constituent atoms, E^e was the energy of free electrons on the hydrogen scale (~4.5 eV), and E_g was the band gap energy of the photocatalyst. The X values for BiOCl was calculated to be 6.33,[52] and E_g was 3.3 eV acquired from DRS analysis (Figure

DOI: 10.1021/acsami.5b05268
ACS Appl. Mater. Interfaces 2015, 7, 20111−20123

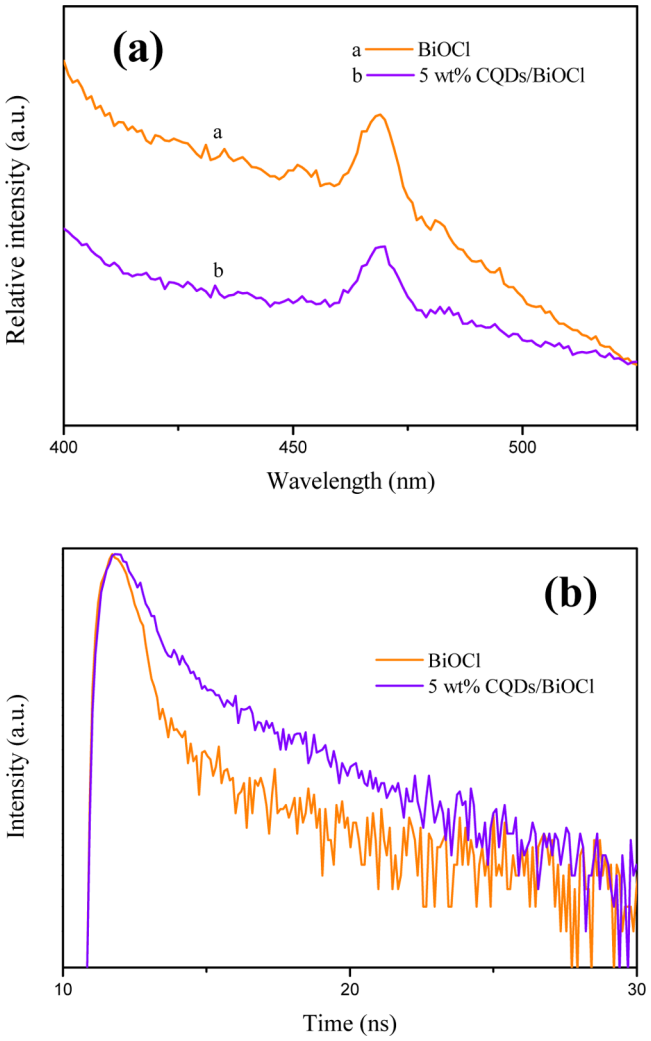

Figure 9. (a) Steady-state PL spectra and (b) time-resolved transient PL decay for pure BiOCl and the 5 wt % CQDs/BiOCl materials.

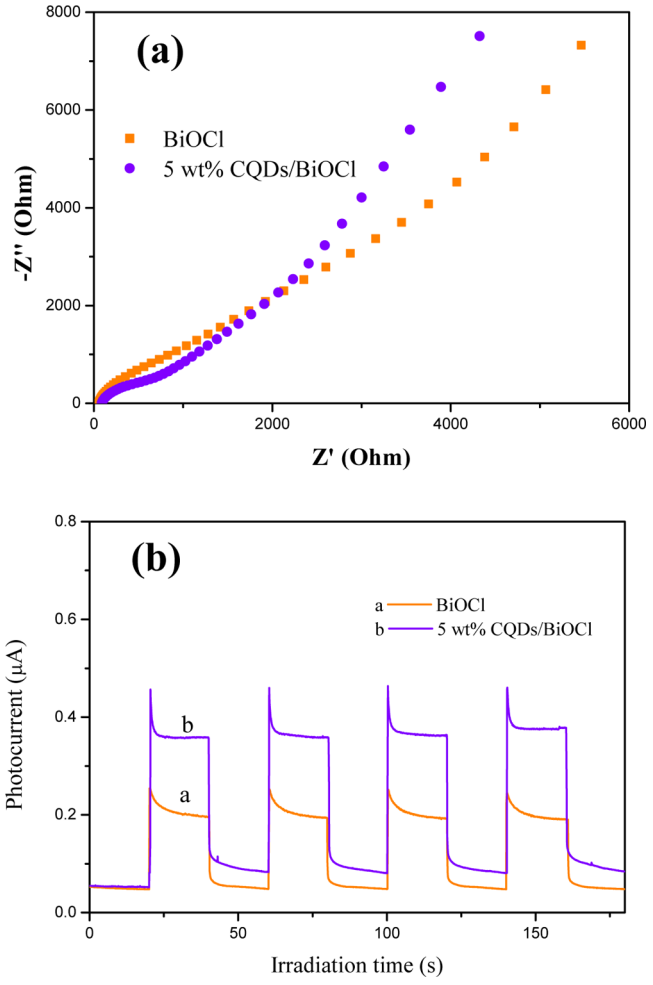

Figure 10. (a) Transient photocurrent response and (b) electrochemical impedance spectra for pure BiOCl and 5 wt % CQDs/BiOCl materials.

S3). Moreover, the CB potential can be obtained by the formula $E_{CB} = E_{VB} - E_g$. Thus, the E_{VB} of BiOCl was calculated to be 3.48 eV and the E_{CB} was 0.18 eV. In this system, the $O_2^{\bullet-}$ and h^+ were determined to be the main active species for the photocatalytic degradation by using ESR analysis (Figure 11) and active species trapping experiments (Figure 12). The characteristic signals of the DMPO-hydroxyl radical (·OH) could not be seen by ESR analysis. And the ·OH was also determined not the main reactive species by trapping experiments. If we use the E_{VB} (3.48 eV) value obtained by empirical equation: $E_{VB} = X - E^e + 0.5E_g$. This VB value (3.48 eV) was more positive than $E^0(\cdot OH/OH^-)$ (2.38 eV vs NHE),[53] and the OH^- can be oxidized to yield ·OH by the h_{VB}^+. At the same time, the electrons in the E_{CB} (0.18 eV) obtained by this method cannot reduce O_2 to generate $O_2^{\bullet-}$ due to the $E^0(O_2/O_2^{\bullet-})$ was about −0.046 eV (vs NHE).[54,55] However, this was inconsistent with the ESR analysis and free radicals trapping experiments in this system.

To gain further insight into the intrinsic reasons that the as-prepared BiOCl can exhibit the visible light photocatalytic activity and the incompatible result above-mentioned, the XPS valence spectra was employed. In XPS valence spectra, the information on the total density of states (DOS) of extra electronic states above the valence band of semiconductor can be obtained.[56] The method to determine the occupied electronic density of states by using the XPS VB spectra was developed recent years for the new-type semiconductors such as $C_3N_{4-x}S_x$,[57] C-, N-, and S-Doped TiO_2[56] as well as black hydrogenated TiO_2.[58] In this system, the highest occupied electronic density of states was measured to be 1.35 eV for as-prepared BiOCl material by XPS valence spectra (Figure 13b). For the CQDs/BiOCl material, the similar result can be acquired (Figure 13a), which implying the CQDs introduction did not affect the electronic density of states of BiOCl matrix. The CQDs have not doping into the BiOCl but only existed in the form of surface modification for efficient transfer electrons. In previous research, the defects states of BiOCl nanosheets can be found by using positron annihilation spectra.[9] This defects states retain three or four negative charges. Zhang's study found that the electronegative defects states can be excited by visible light.[59]

In this system, this highest occupied electronic density of states was come from the defect states. When the CQDs/BiOCl material was irradiated by visible light, the electrons in the defects states can be excited (Figure S4). Due to the cutoff filter we used of Xe lamp was 400 nm for visible light with the corresponding energy about 3.1 eV, the photoinduced electrons was exciting up to a reformed higher CB potential about −1.75 eV (1.35−3.1 eV), which was sufficient to reduce O_2 to

DOI: 10.1021/acsami.5b05268
ACS Appl. Mater. Interfaces 2015, 7, 20111−20123

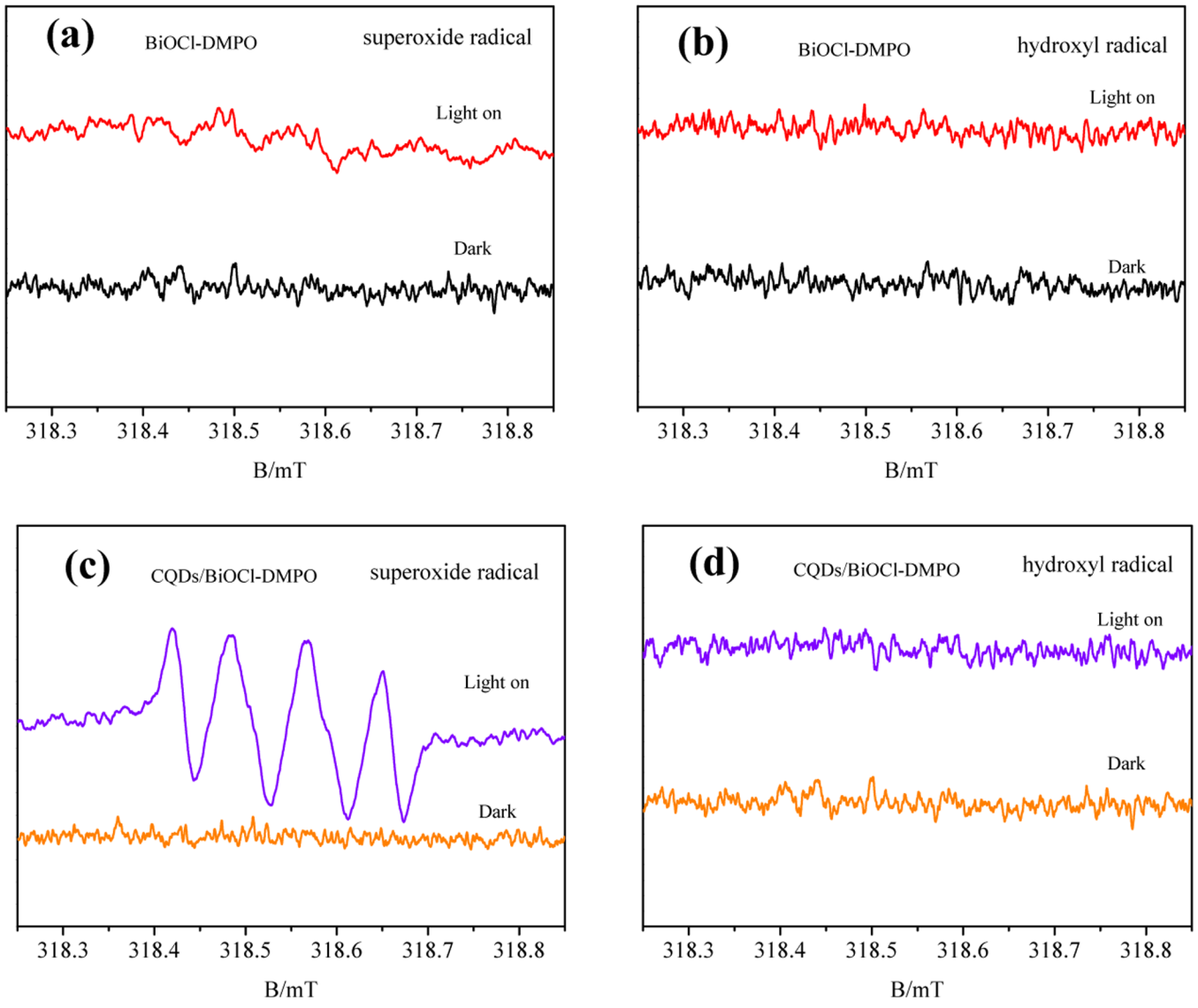

Figure 11. DMPO spin-trapping ESR spectra recorded with (a, b) pure BiOCl and (c, d) 5 wt % CQDs/BiOCl samples in (a, c) methanol dispersion (for DMPO-$O_2^{\bullet-}$) and (b, d) aqueous dispersion (for DMPO-·OH) under visible light irradiation.

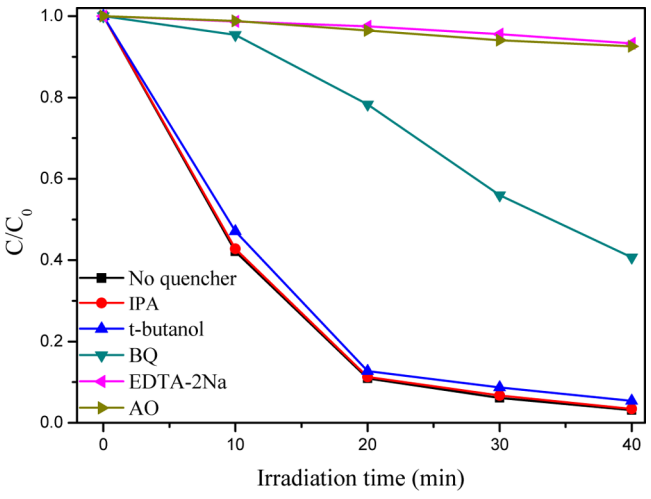

Figure 12. Comparison of photocatalytic activities of 5 wt % CQDs/BiOCl materials for the degradation of RhB with or without adding IPA, *t*-butanol, BQ, EDTA-2Na, and AO under visible light irradiation.

generate $O_2^{\bullet-}$.[51] When no CQDs was introduced, the excited high-energy electrons will rapid decay, transfer to the bottom of the CB of BiOCl and then recombine with holes, thus only a portion of charges could participate in the photocatalytic process. For this reason, the characteristic peaks of DMPO-$O_2^{\bullet-}$ for pure BiOCl materials was feebly. After the CQDs was introduced, the excited high-energy electrons could spatial transfer to the CQDs quickly and form efficient electron−hole pair separation.[60] The high efficient separated high-energy electrons on the CQDs could react with O_2 to produce more $O_2^{\bullet-}$ and the CQDs acted as catalytic active sites. The generated $O_2^{\bullet-}$ and the holes would play important role in the photodegradation process, resulting in excellent photocatalytic activity.

4. CONCLUSIONS

In summary, a novel CQDs modified BiOCl ultrathin nanosheets photocatalyst was synthesized via a facile solvothermal method. The CQDs were assembled on the surface BiOCl ultrathin nanosheets and tight junctions were

DOI: 10.1021/acsami.5b05268
ACS Appl. Mater. Interfaces 2015, 7, 20111−20123

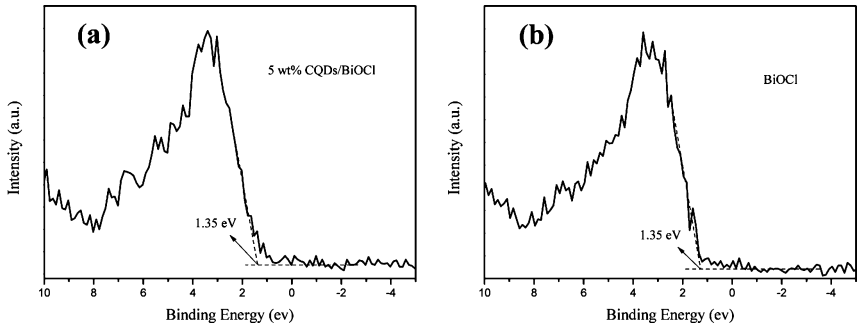

Figure 13. Valence-band XPS spectra of the (a) 5 wt % CQDs/BiOCl and (b) BiOCl materials.

formed. After the introduction of CQDs, the CQDs/BiOCl materials displayed enhanced photocatalytic activities on BPA and RhB degradation under ultraviolet, visible, and near-infrared light irradiation, respectively. The crucial role of CQDs for the improved photocatalytic activity was mainly attributed to the superior electron transfer ability, enhanced light harvesting and boosted catalytic active sites. The main active species were determined to be hole and $O_2^{\bullet-}$ under visible light irradiation by ESR analysis, XPS valence spectra and free radicals trapping experiments.

■ ASSOCIATED CONTENT

Supporting Information

The Supporting Information is available free of charge on the ACS Publications website at DOI: 10.1021/acsami.5b05268.

Cycling experiment for the photodegradation of RhB, mapping images of 5 wt % CQDs/BiOCl materials, $(\alpha E_{photon})^{1/2}$ vs E_{photon} curves of pure BiOCl, photocatalytic mechanism diagram of CQDs/BiOCl material, and pseudo-first-order rate constant for RhB photodegradation (PDF)

■ AUTHOR INFORMATION

Corresponding Authors

*Tel.:+86-511-88791108. Fax: +86-511-88791108. E-mail address: xjx@ujs.edu.cn (J.X.).
*E-mail: lhm@ujs.edu.cn (H.L.).

Notes

The authors declare no competing financial interest.

■ ACKNOWLEDGMENTS

This work was financially supported by the National Nature Science Foundation of China (no. 21206060, 21476098 and 21471069), Jiangsu Province (1102118C), and the Special Financial Grant from the China Postdoctoral Science Foundation (2013T60506).

■ REFERENCES

(1) Bonaccorso, F.; Colombo, L.; Yu, G. H.; Stoller, M.; Tozzini, V.; Ferrari, A. C.; Ruoff, R. S.; Pellegrini, V. Graphene, Related Two-Dimensional Crystals, and Hybrid Systems for Energy Conversion and Storage. *Science* **2015**, *347*, 1246501.

(2) Sun, Y. F.; Gao, S.; Xie, Y. Atomically-Thick Two-Dimensional Crystals: Electronic Structure Regulation and Energy Device Construction. *Chem. Soc. Rev.* **2014**, *43*, 530−546.

(3) Huang, X.; Tan, C. L.; Yin, Z. Y.; Zhang, H. 25th Anniversary Article: Hybrid Nanostructures Based on Two-Dimensional Nanomaterials. *Adv. Mater.* **2014**, *26*, 2185−2204.

(4) Sun, Y. F.; Sun, Z. H.; Gao, S.; Cheng, H.; Liu, Q. H.; Piao, J. Y.; Yao, T.; Wu, C. Z.; Hu, S. L.; Wei, S. Q.; Xie, Y. Fabrication of Flexible and Freestanding Zinc Chalcogenide Single Layers. *Nat. Commun.* **2012**, *3*, 1057.

(5) Li, J.; Yu, Y.; Zhang, L. Z. Bismuth Oxyhalide Nanomaterials: Layered Structures Meet Photocatalysis. *Nanoscale* **2014**, *6*, 8473−8488.

(6) Jiang, J.; Zhao, K.; Xiao, X. Y.; Zhang, L. Z. Synthesis and Facet-Dependent Photoreactivity of BiOCl Single-Crystalline Nanosheets. *J. Am. Chem. Soc.* **2012**, *134*, 4473−4476.

(7) Hu, J. L.; Fan, W. J.; Ye, W. Q.; Huang, C. J.; Qiu, X. Q. Insights into the Photosensitivity Activity of BiOCl under Visible Light Irradiation. *Appl. Catal., B* **2014**, *158−159*, 182−189.

(8) Zhao, K.; Zhang, L. Z.; Wang, J. J.; Li, Q. X.; He, W. W.; Yin, J. J. Surface Structure-Dependent Molecular Oxygen Activation of BiOCl Single-Crystalline Nanosheets. *J. Am. Chem. Soc.* **2013**, *135*, 15750−15753.

(9) Guan, M. L.; Xiao, C.; Zhang, J.; Fan, S. J.; An, R.; Cheng, Q. M.; Xie, J. F.; Zhou, M.; Ye, B. J.; Xie, Y. Vacancy Associates Promoting Solar-Driven Photocatalytic Activity of Ultrathin Bismuth Oxychloride Nanosheets. *J. Am. Chem. Soc.* **2013**, *135*, 10411−10417.

(10) Xiong, J. Y.; Cheng, G.; Li, G. F.; Qin, F.; Chen, R. Well-Crystallized Square-Like 2D BiOCl Nanoplates: Mannitol-Assisted Hydrothermal Synthesis and Improved Visible-Light-Driven Photocatalytic Performance. *RSC Adv.* **2011**, *1*, 1542−1553.

(11) Ye, L. Q.; Zan, L.; Tian, L. H.; Peng, T. Y.; Zhang, J. J. The {001} Facets-Dependent High Photoactivity of BiOCl Nanosheets. *Chem. Commun.* **2011**, *47*, 6951−6953.

(12) Zhang, X.; Wang, X. B.; Wang, L. W.; Wang, W. K.; Long, L. L.; Li, W. W.; Yu, H. Q. Synthesis of a Highly Efficient BiOCl Single-Crystal Nanodisk Photocatalyst with Exposing {001} Facets. *ACS Appl. Mater. Interfaces* **2014**, *6*, 7766−7772.

(13) Li, H.; Zhang, L. Z. Oxygen Vacancy Induced Selective Silver Deposition on the {001} Facets of BiOCl Single-Crystalline Nanosheets for Enhanced Cr(VI) and Sodium Pentachlorophenate Removal under Visible Light. *Nanoscale* **2014**, *6*, 7805−7810.

(14) Yu, Y.; Cao, C. Y.; Liu, H.; Li, P.; Wei, F. F.; Jiang, Y.; Song, W. G. A Bi/BiOCl Heterojunction Photocatalyst with Enhanced Electron-Hole Separation and Excellent Visible Light Photodegrading Activity. *J. Mater. Chem. A* **2014**, *2*, 1677−1681.

(15) Lin, H. X.; Ding, L. Y.; Pei, Z. X.; Zhou, Y. G.; Long, J. L.; Deng, W. H.; Wang, X. X. Au Deposited BiOCl with Different Facets: on Determination of the Facet-Induced Transfer Preference of Charge Carriers and the Different Plasmonic Activity. *Appl. Catal., B* **2014**, *160−161*, 98−105.

(16) Cheng, H. F.; Huang, B. B.; Qin, X. Y.; Zhang, X. Y.; Dai, Y. A Controlled Anion Exchange Strategy to Synthesize Bi_2S_3 Nanocrystals/BiOCl Hybrid Architectures with Efficient Visible Light Photoactivity. *Chem. Commun.* **2012**, *48*, 97−99.

(17) Li, F. T.; Wang, Q.; Wang, X. J.; Li, B.; Hao, Y. J.; Liu, R. H.; Zhao, D. S. In-Situ One-Step Synthesis of Novel BiOCl/$Bi_{24}O_{31}Cl_{10}$ Heterojunctions via Self-Combustion of Ionic Liquid with Enhanced Visible-Light Photocatalytic Activities. *Appl. Catal., B* **2014**, *150−151*, 574−584.

DOI: 10.1021/acsami.5b05268
ACS Appl. Mater. Interfaces 2015, 7, 20111−20123

(18) He, Z. Q.; Shi, Y. Q.; Gao, C.; Wen, L. N.; Chen, J. M.; Song, S. $BiOCl/BiVO_4$ p-n Heterojunction with Enhanced Photocatalytic Activity under Visible-Light Irradiation. *J. Phys. Chem. C* **2014**, *118*, 389−398.
(19) Huang, Z. F.; Song, J. J.; Pan, L.; Jia, X.; Li, Z.; Zou, J. J.; Zhang, X. W.; Wang, L. $W_{18}O_{49}$ Nanowire Alignments with A BiOCl Shell as an Efficient Photocatalyst. *Nanoscale* **2014**, *6*, 8865−8872.
(20) Zhang, X. C.; Guo, T. Y.; Wang, X. W.; Wang, Y. W.; Fan, C. M.; Zhang, H. Facile Composition-Controlled Preparation and Photocatalytic Application of $BiOCl/Bi_2O_2CO_3$ Nanosheets. *Appl. Catal., B* **2014**, *150−151*, 486−495.
(21) Sun, Y. F.; Cheng, H.; Gao, S.; Sun, Z. H.; Liu, Q. H.; Liu, Q.; Lei, F. C.; Yao, T.; He, J. F.; Wei, S. Q.; Xie, Y. Freestanding Tin Disulfide Single-Layers Realizing Efficient Visible-Light Water Splitting. *Angew. Chem., Int. Ed.* **2012**, *51*, 8727−8731.
(22) Lim, S. Y.; Shen, W.; Gao, Z. Q. Carbon Quantum Dots and Their Applications. *Chem. Soc. Rev.* **2015**, *44*, 362−381.
(23) Li, H. T.; Kang, Z. H.; Liu, Y.; Lee, S. T. Carbon Nanodots: Synthesis, Properties and Applications. *J. Mater. Chem.* **2012**, *22*, 24230−24253.
(24) Tian, J.; Leng, Y. H.; Zhao, Z. H.; Xia, Y.; Sang, Y. H.; Hao, P.; Zhan, J.; Li, M. C.; Liu, H. Carbon Quantum Dots/Hydrogenated TiO_2 Nanobelt Heterostructures and Their Broad Spectrum Photocatalytic Properties under UV, Visible, and Near-Infrared Irradiation. *Nano Energy* **2015**, *11*, 419−427.
(25) Li, H. T.; He, X. D.; Kang, Z. H.; Huang, H.; Liu, Y.; Liu, J. L.; Lian, S. Y.; Tsang, C. H. A.; Yang, X. B.; Lee, S. T. Water-Soluble Fluorescent Carbon Quantum Dots and Photocatalyst Design. *Angew. Chem., Int. Ed.* **2010**, *49*, 4430−4434.
(26) Zhang, X.; Wang, F.; Huang, H.; Li, H. T.; Han, X.; Liu, Y.; Kang, Z. H. Carbon Quantum Dot Sensitized TiO_2 Nanotube Arrays for Photoelectrochemical Hydrogen Generation under Visible Light. *Nanoscale* **2013**, *5*, 2274−2278.
(27) Yu, H. J.; Zhao, Y. F.; Zhou, C.; Shang, L.; Peng, Y.; Cao, Y. H.; Wu, L. Z.; Tung, C. H.; Zhang, T. R. Carbon Quantum Dots/TiO_2 Composites for Efficient Photocatalytic Hydrogen Evolution. *J. Mater. Chem. A* **2014**, *2*, 3344−3351.
(28) Zhang, H. C.; Huang, H.; Ming, H.; Li, H. T.; Zhang, L. L.; Liu, Y.; Kang, Z. H. Carbon Quantum Dots/Ag_3PO_4 Complex Photocatalysts with Enhanced Photocatalytic Activity and Stability under Visible Light. *J. Mater. Chem.* **2012**, *22*, 10501−10506.
(29) Liu, J.; Liu, Y.; Liu, N. Y.; Han, Y. Z.; Zhang, X.; Huang, H.; Lifshitz, Y.; Lee, S. T.; Zhong, J.; Kang, Z. H. Metal-Free Efficient Photocatalyst for Stable Visible Water Splitting via a Two-Electron Pathway. *Science* **2015**, *347*, 970−974.
(30) Li, H. T.; Liu, R. H.; Liu, Y.; Huang, H.; Yu, H.; Ming, H.; Lian, S. Y.; Lee, S. T.; Kang, Z. H. Carbon Quantum Dots/Cu_2O Composites with Protruding Nanostructures and their Highly Efficient (Near) Infrared Photocatalytic Behavior. *J. Mater. Chem.* **2012**, *22*, 17470−17475.
(31) Di, J.; Xia, J. X.; Ge, Y. P.; Li, H. P.; Ji, H. Y.; Xu, H.; Zhang, Q.; Li, H. M.; Li, M. N. Novel Visible-Light-Driven CQDs/Bi_2WO_6 Hybrid Materials with Enhanced Photocatalytic Activity toward Organic Pollutants Degradation and Mechanism Insight. *Appl. Catal., B* **2015**, *168−169*, 51−61.
(32) Hou, Y. D.; Laursen, A. B.; Zhang, J. S.; Zhang, G. G.; Zhu, Y. S.; Wang, X. C.; Dahl, S.; Chorkendorff, I. Layered Nanojunctions for Hydrogen-Evolution Catalysis. *Angew. Chem., Int. Ed.* **2013**, *52*, 3621−3625.
(33) Yu, C. L.; Li, G.; Kumar, S.; Yang, K.; Jin, R. C. Phase Transformation Synthesis of Novel Ag_2O/Ag_2CO_3 Heterostructures with High Visible Light Efficiency in Photocatalytic Degradation of Pollutants. *Adv. Mater.* **2014**, *26*, 892−898.
(34) Yu, C. L.; Yang, K.; Xie, Y.; Fan, Q. Z.; Yu, J. C.; Shu, Q.; Wang, C. Y. Novel Hollow Pt-ZnO Nanocomposite Microspheres with Hierarchical Structure and Enhanced Photocatalytic Activity and Stability. *Nanoscale* **2013**, *5*, 2142−2151.
(35) Yu, C. L.; Wei, L. F.; Zhou, W. Q.; Chen, J. C.; Fan, Q. Z.; Liu, H. Enhancement of the Visible Light Activity and Stability of Ag_2CO_3 by Formation of AgI/Ag_2CO_3 Heterojunction. *Appl. Surf. Sci.* **2014**, *319*, 312−318.
(36) Yu, C. L.; Li, G.; Kumar, S.; Kawasaki, H.; Jin, R. C. Stable $Au_{25}(SR)_{18}/TiO_2$ Composite Nanostructure with Enhanced Visible Light Photocatalytic Activity. *J. Phys. Chem. Lett.* **2013**, *4*, 2847−2852.
(37) Yu, C. L.; Wei, L. F.; Chen, J. C.; Xie, Y.; Zhou, W. Q.; Fan, Q. Z. Enhancing the Photocatalytic Performance of Commercial TiO_2 Crystals by Coupling with Trace Narrow-Band-Gap Ag_2CO_3. *Ind. Eng. Chem. Res.* **2014**, *53*, 5759−5766.
(38) Zhu, S. J.; Meng, Q. N.; Wang, L.; Zhang, J. H.; Song, Y. B.; Jin, H.; Zhang, K.; Sun, H. C.; Wang, H. Y.; Yang, B. Highly Photoluminescent Carbon Dots for Multicolor Patterning, Sensors, and Bioimaging. *Angew. Chem., Int. Ed.* **2013**, *52*, 3953−3957.
(39) Di, J.; Xia, J. X.; Ji, M. X.; Li, H. P.; Xu, H.; Li, H. M.; Chen, R. The Synergistic Role of Carbon Quantum Dots for the Improved Photocatalytic Performance of Bi_2MoO_6. *Nanoscale* **2015**, *7*, 11433−11443.
(40) Xiao, X.; Hao, R.; Liang, M.; Zuo, X. X.; Nan, J. M.; Li, L. S.; Zhang, W. D. One-Pot Solvothermal Synthesis of Three-Dimensional (3D) BiOI/BiOCl Composites with Enhanced Visible-Light Photocatalytic Activities for the Degradation of Bisphenol-A. *J. Hazard. Mater.* **2012**, *233−234*, 122−130.
(41) Di, J.; Xia, J. X.; Yin, S.; Xu, H.; Xu, L.; Xu, Y. G.; He, M. Q.; Li, H. M. Preparation of Sphere-Like g-C_3N_4/BiOI Photocatalysts via a Reactable Ionic Liquid for Visible-Light-Driven Photocatalytic Degradation of Pollutants. *J. Mater. Chem. A* **2014**, *2*, 5340−5351.
(42) Gao, X. H.; Wu, H. B.; Zheng, L. X.; Zhong, Y. J.; Hu, Y.; Lou, X. W. Formation of Mesoporous Heterostructured $BiVO_4/Bi_2S_3$ Hollow Discoids with Enhanced Photoactivity. *Angew. Chem., Int. Ed.* **2014**, *53*, 5917−5921.
(43) Yu, J. G.; Low, J. X.; Xiao, W.; Zhou, P.; Jaroniec, M. Enhanced Photocatalytic CO_2-Reduction Activity of Anatase TiO_2 by Coexposed {001} and {101} Facets. *J. Am. Chem. Soc.* **2014**, *136*, 8839−8842.
(44) Di, J.; Xia, J. X.; Yin, S.; Xu, H.; Xu, L.; Xu, Y. G.; He, M. Q.; Li, H. M. One-Pot Solvothermal Synthesis of Cu-modified BiOCl Via a Cu-containing Ionic Liquid and Its Visible-Light Photocatalytic Properties. *RSC Adv.* **2014**, *4*, 14281−14290.
(45) Wang, S. M.; Li, D. L.; Sun, C.; Yang, S. G.; Guan, Y.; He, H. Synthesis and Characterization of g-C_3N_4/Ag_3VO_4 Composites with Significantly Enhanced Visible-Light Photocatalytic Activity for Triphenylmethane Dye Degradation. *Appl. Catal., B* **2014**, *144*, 885−892.
(46) Leelavathi, A.; Madras, G.; Ravishankar, N. New Insights into Electronic and Geometric Effects in the Enhanced Photoelectrooxidation of Ethanol Using ZnO Nanorod/Ultrathin Au Nanowire Hybrids. *J. Am. Chem. Soc.* **2014**, *136*, 14445−14455.
(47) Zhu, Y. R.; Ji, X. B.; Pan, C. C.; Sun, Q. Q.; Song, W. X.; Fang, L. B.; Chen, Q. Y.; Banks, C. E. A Carbon Quantum Dot Decorated RuO_2 Network: Outstanding Supercapacitances under Ultrafast Charge and Discharge. *Energy Environ. Sci.* **2013**, *6*, 3665−3675.
(48) Di, J.; Xia, J. X.; Yin, S.; Xu, H.; He, M. Q.; Li, H. M.; Xu, L.; Jiang, Y. P. A g-C_3N_4/BiOBr Visible-Light-Driven Composite: Synthesis via a Reactable Ionic Liquid and Improved Photocatalytic Activity. *RSC Adv.* **2013**, *3*, 19624−19631.
(49) Lv, Y. H.; Zhu, Y. Y.; Zhu, Y. F. Enhanced Photocatalytic Performance for the $BiPO_{4-x}$ Nanorod Induced by Surface Oxygen Vacancy. *J. Phys. Chem. C* **2013**, *117*, 18520−18528.
(50) Di, J.; Xia, J. X.; Ge, Y. P.; Xu, L.; Xu, H.; He, M. Q.; Zhang, Q.; Li, H. M. Reactable Ionic Liquid-Assisted Rapid Synthesis of BiOI Hollow Microspheres at Room Temperature with Enhanced Photocatalytic Activity. *J. Mater. Chem. A* **2014**, *2*, 15864−15874.
(51) Zhang, X.; Zhang, L. Z.; Xie, T. F.; Wang, D. J. Low-Temperature Synthesis and High Visible-Light-Induced Photocatalytic Activity of $BiOI/TiO_2$ Heterostructures. *J. Phys. Chem. C* **2009**, *113*, 7371−7378.
(52) Ye, L. Q.; Liu, J. Y.; Gong, C. Q.; Tian, L. H.; Peng, T. Y.; Zan, L. Two Different Roles of Metallic Ag on Ag/AgX/BiOX (X = Cl, Br) Visible Light Photocatalysts: Surface Plasmon Resonance and Z-Scheme Bridge. *ACS Catal.* **2012**, *2*, 1677−1683.

DOI: 10.1021/acsami.5b05268
ACS Appl. Mater. Interfaces 2015, 7, 20111−20123

(53) Cheng, H. F.; Huang, B. B.; Dai, Y.; Qin, X. Y.; Zhang, X. Y. One-Step Synthesis of the Nanostructured AgI/BiOI Composites with Highly Enhanced Visible-Light Photocatalytic Performances. *Langmuir* **2010**, *26*, 6618−6624.
(54) Ye, L. Q.; Chen, J. N.; Tian, L. H.; Liu, J. Y.; Peng, T. Y.; Deng, K. J.; Zan, L. BiOI Thin Film via Chemical Vapor Transport: Photocatalytic Activity, Durability, Selectivity and Mechanism. *Appl. Catal., B* **2013**, *130*, 1−7.
(55) Chen, C. C.; Ma, W. H.; Zhao, J. C. Semiconductor-Mediated Photodegradation of Pollutants under Visible-Light Irradiation. *Chem. Soc. Rev.* **2010**, *39*, 4206−4219.
(56) Chen, X. B.; Burda, C. The Electronic Origin of the Visible-Light Absorption Properties of C-, N- and S-Doped TiO_2 Nanomaterials. *J. Am. Chem. Soc.* **2008**, *130*, 5018−5019.
(57) Liu, G.; Niu, P.; Sun, C. H.; Smith, S. C.; Chen, Z. G.; Lu, G. Q.; Cheng, H. M. Unique Electronic Structure Induced High Photoreactivity of Sulfur-Doped Graphitic C_3N_4. *J. Am. Chem. Soc.* **2010**, *132*, 11642−11648.
(58) Chen, X. B.; Liu, L.; Yu, P. Y.; Mao, S. S. Increasing Solar Absorption for Photocatalysis with Black Hydrogenated Titanium Dioxide Nanocrystals. *Science* **2011**, *331*, 746−750.
(59) Li, H.; Shi, J. G.; Zhao, K.; Zhang, L. Z. Sustainable Molecular Oxygen Activation with Oxygen Vacancies on the {001} Facets of BiOCl Nanosheets under Solar Light. *Nanoscale* **2014**, *6*, 14168−14173.
(60) Xie, M. Z.; Fu, X. D.; Jing, L. Q.; Luan, P.; Feng, Y. J.; Fu, H. G. Long-Lived, Visible-Light-Excited Charge Carriers of TiO_2/$BiVO_4$ Nanocomposites and their Unexpected Photoactivity for Water Splitting. *Adv. Energy Mater.* **2014**, *4*, 1300995.

DOI: 10.1021/acsami.5b05268
ACS Appl. Mater. Interfaces 2015, 7, 20111−20123